Available online at www.sciencedirect.com
SCIENCE DIRECT
ELSEVIER
European Journal of Mechanics B/Fluids 25 (2006) 321–336
EUROPEAN JOURNAL OF MECHANICS B/FLUIDS

Hydrodynamic forces acting on a rigid fixed sphere in early transitional regimes

G. Bouchet *, M. Mebarek, J. Dušek

Institut de Mécanique des Fluides et des Solides, 2, rue Boussingault, 67000 Strasbourg, France

Received 13 June 2005; received in revised form 15 September 2005; accepted 12 October 2005

Available online 28 November 2005

Abstract

A spectral – spectral-element code is used to investigate the hydrodynamic forces acting on a fixed sphere placed in a uniform flow in the Reynolds number interval [10–320] covering the early stages of transition, i.e. the steady axisymmetric regime with detached flow, the steady non-axisymmetric and the unsteady periodic regimes of the sphere wake. The mentioned changes of regimes, shown by several authors to be related to a regular and a Hopf bifurcations in the wake, result in significant changes of hydrodynamic action of the flow on the sphere. In the present paper, we show that the loss of axisymmetry is accompanied not only by an onset of lift but also of a torque and we give accurate values of drag, lift and torque in the whole interval of investigated Reynolds numbers. Among other results show, moreover, that each bifurcation is accompanied also by a change of the trend of the drag versus Reynolds number dependence, the overall qualitative effect of instabilities being an increase of drag.

Keywords: Sphere; Wake; Forces; Instabilities

1. Introduction

Large amount of recent numerical and theoretical work [1–5] has been focused on the investigation of instabilities responsible for the transition of the sphere wake to turbulence. It has been shown that this transition is accompanied by a symmetry breaking setting in at the primary, regular, i.e. steady to steady, bifurcation whereby axisymmetry gives way to a plane symmetry with an arbitrarily chosen plane direction. A wide consensus allows to place the critical Reynolds number (based on the asymptotic flow velocity U_∞ and the sphere diameter d, $Re = U_\infty d/\nu$, ν being the kinematic viscosity of the fluid) at $Re_1 = 212$. The transition of the steady regime to an unsteady periodic one is triggered by a Hopf bifurcation at a critical Reynolds number found in [5,6] to be $Re_2 = 273$. The obtained results have a fundamental importance for the understanding of the transition from a steady and axisymmetric regime to a non-axisymmetric and unsteady state of the wake. Relatively little interest has been so far given to the way how the instabilities change the hydrodynamic forces acting on the sphere. In spite of the fact that the knowledge of hydrodynamic forces is not necessary for the understanding of wake instabilities as long as the sphere is kept fixed, the issue of hydrodynamic forces acting on a sphere is of greatest historical and practical interest. Moreover, in the transitional

* Corresponding author. Tel.: +33 (0)3 90 24 28 95; fax: +33 (0)3 88 61 43 00.
E-mail address: bouchet@imfs.u-strasbg.fr (G. Bouchet).

0997-7546/$ – see front matter
doi:10.1016/j.euromechflu.2005.10.001

(dynamically low dimensional) regimes they provide a good characteristic of the wake as a dynamical system. The calculation of the sphere drag was probably the first, and for a long time the only, problem consisting in solving the full problem of flow equations and hydrodynamic forces. Except for infinitely low particle Reynolds numbers (typically up to $Re = 0.5$) where the Stokes approximation applies [7] and for Reynolds numbers on the order of one, for which the theoretical Oseen's solution is satisfactory, the drag versus Reynolds number laws are empirical results of much experimental data used to extrapolate the only available theoretical results to higher Reynolds numbers. The well known laws [8,9] provide satisfactory agreement with experiments and numerical results up to $Re \approx 200$. Beyond 200, there are two basic reasons why these laws fail to be satisfactory. Firstly, though assuming the flow past the sphere axisymmetric, these laws have been found to present an increasing error beyond $Re = 200$ if compared to axisymmetric numerical simulations (6% of error is stated by [10] for the law established by [8]). Secondly, and more importantly, the empirical laws based on the assumption that the hydrodynamic action of the flow on spherical body is isotropic and are described by a smooth function of the Reynolds number fail to account for well known effects due to axisymmetry breaking and transition to unsteadiness in the sphere wake. The best evidence of anisotropy of the hydrodynamic force is probably due to Johnson and Patel [4] who computed the lift force arising above the primary (axisymmetry breaking) instability threshold at $Re = 250$ and $Re = 300$. This force lies in the symmetry plane selected by the bifurcation and its magnitude was found to be a little less than 10% of the drag at $Re = 250$ and roughly 10% of the drag at $Re = 300$. The onset of unsteadiness results, naturally, in an unsteadiness of drag and lift.

The purpose of the present paper is to provide a systematic study of hydrodynamic forces acting on a fixed sphere in a wide interval of Reynolds numbers starting with the flow detachment going up to the upper bound of the unsteady periodic regime. The numerical simulations are carried out using the spectral – spectral-element code described in Ghidersa and Dušek [5]. Additional validation and accuracy estimations are presented throughout the paper, namely in Sections 3, 5 and 7. They are based on the numerical convergence of investigated physical quantities such as the drag, the axisymmetry breaking threshold and the amplitude of the oscillations in the unsteady periodic regime. The drag in the axisymmetric regime computed between $Re = 20$ and $Re = 210$ is presented in Section 4. The results concerning the steady non-axisymmetric regime are given in Section 6. A special attention is paid to the torque. Results relative to the unsteady regime are given in Section 7.

2. Theory and numerical method

In this section, we present a summary of the mathematical formulation and numerical method used in this study. For more details refer to Tomboulides et al. [3] and Ghidersa and Dušek [5].

2.1. Mathematical formulation

We consider the unsteady flow of an incompressible fluid of density ρ and dynamical viscosity μ around a sphere of diameter d. We use the cylindrical coordinate system (z, r, θ), the *z-axis* being parallel to the uniform inflow direction U_∞. The coordinates are non-dimensionalized with respect to the length scale d. The axial, radial and azimuthal velocities in this system, denoted respectively by (u, v, w), are non-dimensionalized with respect to the inflow velocity U_∞. The pressure p is non-dimensionalized with respect to ρU_∞^2; the dimensionless time is $t = d/U_\infty$.

With these variables, the Navier–Stokes equations are expressed as the following system of equations:

$$\frac{\partial \vec{v}}{\partial t} + (\vec{v} \cdot \vec{\nabla})\vec{v} = -\vec{\nabla} p + \nu \nabla^2 \vec{v}, \tag{1}$$

$$\nabla \cdot \vec{v} = 0 \tag{2}$$

where $\nu = 1/Re$ stands for the inverse of the Reynolds number $Re = U_\infty d\rho/\mu$. For non-swirling axisymmetric flows, the flow field solution of (1) and (2) is independent of θ and has no azimuthal velocity component.

The linear stability analysis of an axisymmetric flow field $(\vec{V}, P)$ consists in introducing an infinitesimal perturbation $(\vec{v}', p')$:

$$\vec{v} = \vec{V} + \vec{v}',$$

$$p = P + p'.$$

This perturbation is expressed via complex eigenmodes $\vec{\Phi}, \Pi$:

$$\vec{v}' = \alpha\, \mathrm{e}^{\lambda t}\vec{\Phi} + c.c,$$
$$p' = \alpha\, \mathrm{e}^{\lambda t}\Pi + c.c,$$
$$\vec{\Phi} = (\phi_r, \phi_\theta, \phi_z).$$

α being an arbitrary complex constant and $c.c$ standing for the complex conjugate.

Depending on the solution of the eigenvalue problem

$$\lambda\vec{\Phi} + \mathcal{L}[\vec{v}] + \vec{\nabla}(\Pi) = 0, \tag{3}$$
$$\nabla \cdot \vec{\Phi} = 0 \tag{4}$$

the perturbation is either amplified or damped. As explained in [5], the axisymmetry of the base flow and the absence of swirl allow to rewrite the eigenvalue problem (3) and (4) as a sequence of projections to subspaces of perturbations characterized by an absolute value of the azimuthal wave number m (eigen-subspaces of the rotation operator $\frac{\partial}{\partial\theta}$).

For the sphere wake, the first instability occurs via a regular bifurcation at $Re \simeq 212$ (real λ) in the subspace with azimuthal wave number $m = 1$ (see [2,3,5]). This triggers the loss of axisymmetry.

The unstable $m = 1$ mode generates, via the non-linear terms of the Navier–Stokes equations, non-linear modes with all azimuthal wavenumbers, as well as a non-linear axisymmetric correction.

As a result, the velocity and pressure are the sums of very rapidly converging series:

$$\vec{v}(r, z, \theta, t) = \sum_{m=-\infty}^{m=+\infty} \sigma(m)\vec{v}_{|m|}(r, z, t)\, \mathrm{e}^{-\mathrm{i}m\theta}, \tag{5}$$

$$p(r, z, \theta, t) = \sum_{m=-\infty}^{m=+\infty} p_m(r, z, t)\, \mathrm{e}^{-\mathrm{i}m\theta} \tag{6}$$

where $\sigma(m) = \mathrm{Diag}(1, 1, -\mathrm{i}\,\mathrm{sgn}(m))$.

2.2. Numerical method

Eqs. (5) and (6) provide a particularly efficient spectral expansion. Inserting (5) and (6) into Eqs. (1), (2) yields a system of coupled two-dimensional (r–z) depending partial differential equations for the azimuthal modes ($\vec{v}_m$, p_m) (see Tomboulides et al. [3] and Ghidersa and Dušek [5] for details). The r–z domain is broken up into K spectral elements (see Patera [11] and Karniadakis [12]), standard high order Lagrangian finite elements, with a variable number N of Gauss–Lobatto–Legendre collocation points in each direction within the spectral element. Only the C^0 continuity condition is required between two elements.

The discretized equations are integrated in time using a semi-implicit method with a fully explicit third order accurate treatment of the non-linear coupling terms and with a full inversion of the Stokes problem in the individual azimuthal eigen-subspaces.

The truncated convolutions of non-linear terms are directly calculated in the Fourier space. In our case, Ghidersa and Dušek [5] showed that for Reynolds numbers lower than 300 a very small number of azimuthal modes yields a very good accuracy, thus making transformations between the physical and the Fourier space unnecessary.

The convergence to the exact solution in the spectral element method is obtained either by increasing the number of macro-elements K, or by increasing the number of collocation points N. In the first case the error decreases algebraically like K^{-N}, where N is fixed. When the number of the spectral-elements K is constant and the polynomial order N increases, the error decreases exponentially as $\mathrm{e}^{-\delta N}$, where δ is constant. The break up into spectral elements allows to distribute the computational effort in an optimal way within the domain. The final accuracy is achieved preferably by increasing the spectral element order.

3. Computational domain, boundary conditions and mesh optimization

3.1. Computational domain

For sphere wakes, cylindrical (Tomboulides et al. [3] and Ghidersa and Dušek [5]) or spherical (Johnson and Patel [4], Mittal [13]) domain topologies are usually used. The advantage of the cylindrical topology consists in the

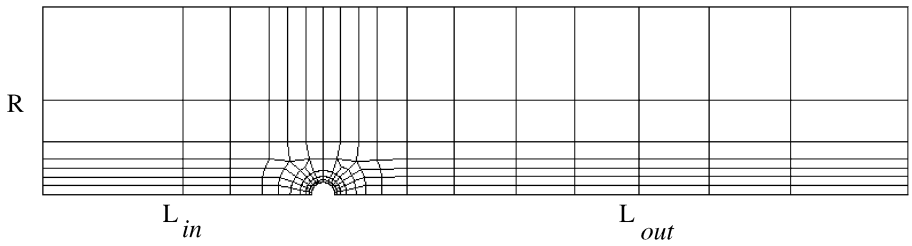

Fig. 1. Computational domain.

fact that, for transitional Reynolds numbers, the wake is confined within a very elongated but rather confined (about twice the sphere radius) cylindrical domain.

The domain radius is denoted R and the total domain length L. The entire domain is obtained by a 2π-rotation of a z–r domain around the flow axis.

The sphere center is placed at the origin of the *z-axis*. Let L_{in} and L_{out} be respectively the upstream and downstream distances between the limits of the numerical domain and the sphere center. Therefore, the overall length is $L = L_{\text{in}} + L_{\text{out}}$. The z–r domain is broken up into spectral-elements with $N \times N$ collocation points (see Fig. 1).

3.2. Boundary conditions

To simulate as exactly as possible the infinite flow on a finite numerical domain, appropriate boundary conditions are required at the upstream and downstream of the domain boundaries. The boundary conditions simulate an inflow in the upstream direction of the cylindrical domain, and an outflow condition on the lateral and downstream limits of the domain; on the sphere surface a no-slip condition is applied. The inflow boundary condition consists in a uniform velocity profile $u = U_\infty,\ v = 0,\ w = 0$; the outflow condition amounts to set both of the pressure and viscous stresses to zero. This outflow condition, imposed in a weak sense, allows the disturbances to leave the domain without reflection and avoid confinement effects of the lateral boundary. The symmetry axis boundary conditions are treated using the complex velocity components of Orszag and Patera [14].

3.3. **Discretization optimization**

The basic issues of discretization optimization are described in Ghidersa and Dušek [5]. This optimization amounts to test the influence of the parameters of the discretization, i.e. of the geometrical parameters, L_{in}, L_{out} and the radius R, of the break up into spectral elements, of the number of azimuthal modes and of the time step on the overall accuracy. Depending on the regime, not all parameters have to be tested in the same time. This allows to test, first, the choice of the 2D spatial discretization parameters on the drag coefficient (see Section 4.1) and on the capture of the primary instability threshold (see Sections 5.2 and 5.4). The number of azimuthal modes becomes of importance in the steady non-axisymmetric regime (see Section 6.1) whereas the time step could influence the results in the unsteady periodic regime. The latter, being determined by a rather restrictive CFL criterion, is, however, so fine (typically 5000 time steps per period) that any further refinement appears to have no effect. Instead, the accuracy of the three-dimensionality representation has a significant impact on the secondary instability and further tests of the azimuthal discretization are given in Section 7.

4. Steady axisymmetric flow

The axisymmetric regime can be simulated by our code by truncating the azimuthal expansion of the Navier–Stokes equations to the axisymmetric $m = 0$ mode. Below the onset of symmetry breaking this solution is stable and corresponds to the observed axisymmetric flow. Above the symmetry breaking threshold, it provides the unperturbed unstable base flow of the instability.

As a check of accuracy of the numerical experimentation, and to ascertain that the essential details of the flow are captured, a numerical investigation of the axisymmetric regime is performed, and compared with previous studies. In the range of Reynolds number [0–210], the flow remains axisymmetric with two different features. For very

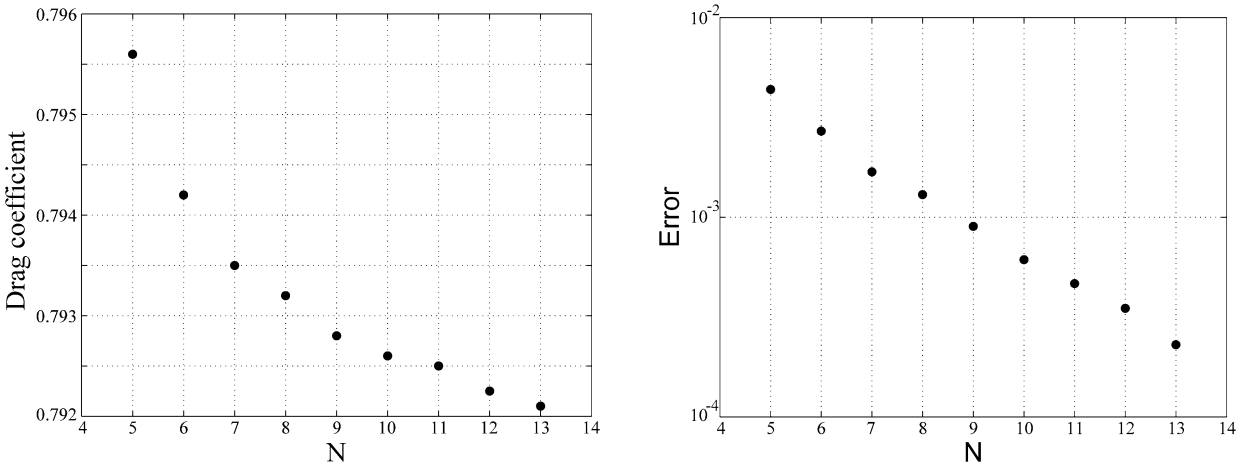

Fig. 2. Drag coefficient and its error with varying number of collocation points.

low Reynolds numbers, the creeping flow exhibits a perfect upstream-downstream symmetry. For higher Reynolds numbers, the flow separates and a vortex forms at the rear stagnation point of the sphere (Magarvey and Bishop [15] and Levi [16]). Flow visualization evidences a rectilinear thread along the flow axis; the critical Reynolds number Re_{rec} for the onset of recirculation is usually given at $Re_{\text{rec}} \approx 20$ (see [4,10,17]). Rimon and Cheng [18] suggest that the critical Reynolds number is $Re_{\text{rec}} = 10$. Experimentally, Taneda [19] detected the apparition of the recirculation structures at $Re_{\text{rec}} = 24$; Nakamura [20] gave a critical Reynolds $Re_{\text{rec}} = 10$ and asserted that this critical number could be lower. The recirculation length and the separation angle measured from the rear stagnation point grow with Reynolds number; both quantities were found to follow an approximately logarithmic relationship with the Reynolds number. Nakamura [20] remarked that the recirculation zone assumed the shapes changing from the concave to the convex form as the Reynolds number increased.

4.1. Numerical tests

The spatial discretization accuracy was tested by increasing the number of collocation points of the pseudo-spectral expansion, and by following its impact on the computed drag. The tests were performed at $Re = 190$.

Fig. 2 shows clearly the quasi-exponential convergence [11] of the drag coefficient when the number of collocation points grows. In the same figure, we have plotted the drag versus N (left graph) and the error with respect to the "accurate" asymptotic value obtained by fitting the drag versus N curve to an exponential. It arises from these figures that a precision of less than 0.1% of the drag value is obtained for 9×9 collocation points in each spectral element. We can note here that the weak difference between the found dependence on N and the theoretically predicted behavior is certainly due to a contribution from the finite size of the domain, and from the finiteness of the number K of macro-elements.

4.2. Simulation results

Using 10×10 collocation points, simulations were performed for Reynolds numbers between 10 and 200. The present results confirm that the onset of development of a standing eddy at the rear of the sphere takes place for Reynolds number lies between 20 and 21. The two quantities which characterize the separated flow past a sphere are the separation angle, measured from the front stagnation point, and the recirculation length. They are displayed in Fig. 3 with respect to the Reynolds number and compared to available experimental measurements of Taneda [19] and Nakamura [20] and to numerical results of Tomboulides et al. [21], Mittal [13], Magnaudet et al. [10] and Bagchi and Balachandar [22]. The results of the present study are in a very good agreement with these numerical and experimental results. For $Re \geqslant 150$ the Taneda's recirculation length is in disagreement with numerical results [10,21,13]. This disagreement is clearly due to an early onset of the first bifurcation in Taneda's measurements; the trend found by Taneda for Reynolds numbers close to 200 is similar to that found for Reynolds numbers above 212 in Fig. 12.

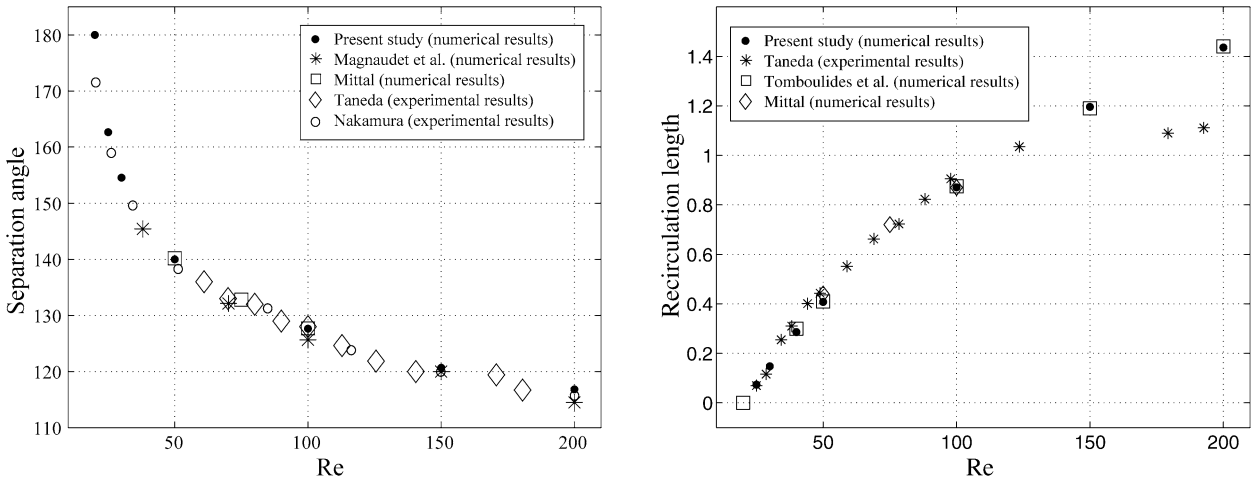

Fig. 3. Separation angle recirculation length and recirculation length for axisymmetric flow with Reynolds number: comparison between experimental and numerical results.

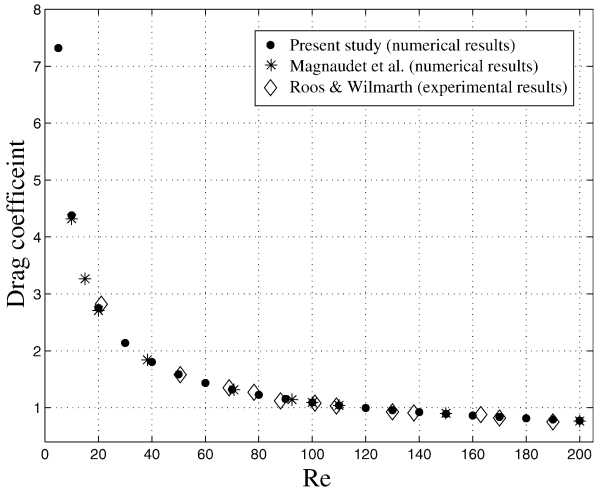

Fig. 4. Drag coefficient versus Reynolds number: comparison between experimental and numerical results.

The values of the present numerical predictions of the drag coefficient C_D, defined by $C_D = 8F_x/\pi D^2 \rho U_\infty^2$, where F_x is the force in the streamwise direction, are summarized in Fig. 4. The drag coefficient C_D is represented versus the Reynolds number in the range of [10–200]. For comparison, these values are plotted on the same graph with the experimental data of Roos and Wilmarth [23] and with the numerical results of Magnaudet et al. [10]. The maximal discrepancy between the present results and that of [10] is of 4%.

It is obvious that there is a noteworthy superimposition of all represented data indicating the high reliability of measurements and simulations of [23] and [10]. Incidentally, it helps to confirm the high accuracy of the present computation.

5. Linear analysis of the axisymmetry breaking

The primary instability is due to a regular bifurcation breaking the axisymmetry but keeping the flow steady. The linear analysis provides an estimation of the instability threshold. Taking advantage of the Fourier development, whereby the individual Fourier modes can be investigated separately, one can easily perform both a linear and a fully non-linear analysis with a variable number of azimuthal modes. The linear mode is computed by truncating the azimuthal mode expansion to just the $m = 1$ mode, while keeping the $m = 0$ mode equal to the base flow. The initial

condition for the linear mode is obtained by perturbing its radial velocity component at a single point. The technical approach is as follows: the steady axisymmetric base flow is first computed by truncating the azimuthal expansion to $m = 0$ (see Section 4). Extreme care was taken to ensure a very good convergence of the steady axisymmetric base flow (see also Section 5.5).

5.1. Instability threshold

As mentioned in Section 2.1, the eigenvalue σ of the linear problem determines the growth of the linear mode and consequently of the instability amplitude. Following the sign of eigenvalue of the linear problem σ, the perturbation is either amplified or damped. Close to the instability threshold, the critical Reynolds number, at which the axisymmetry breaking occurs, can be related to σ by a simple linear interpolation with a very good accuracy. For the present study, a first computation using 6×6 collocation points in the spatial discretization gave a critical Reynolds number $Re_{c_1} = 210.3$ for the regular bifurcation; this value is very close ($\sim$1%) to the actual number estimated in [3,4] and [5].

5.2. Threshold dependence on increasing spatial discretization

In Ghidersa and Dušek [5], an estimate of the accurate critical Reynolds number was made using the linear interdependence between σ and Re, and the dependence of σ on the discretization accuracy. Here we submit this estimate to a more thorough test.

The number of collocation points N in the spatial discretization was increased from 6×6 to 12×12 collocation points, by an increment of 1 (two cases, $N = 8$ and $N = 10$, are presented in Fig. 5). For each discretization, the Reynolds number corresponding to zero amplification rate σ was determined by interpolation ($Re = 211.0$ and $Re = 211.4$, respectively). Fig. 6 represents the values of Re_{c_1} obtained for each N.

It obviously reveals that the values of Re_{c_1} increase with N, and reach an asymptotic value when the precision in each spectral element tends to infinity. The trend fits again very well to an exponential, allowing to estimate the limit value which is the accurate threshold of the transition to steady asymmetric flow. The Re_{c_1} is estimated here at 211.9 which is in perfect agreement of about 0.1% with previous predictions of [3] ($Re_{c_1} = 212$) and [5] ($Re_{c_1} = 212.2$). The monotonous increasing trend of the critical Reynolds number is a characteristic feature of the spectral element method with its only C^0 continuity at the element interfaces. The discontinuity of the flow field derivatives tends to amplify the simulated (physical) instabilities (see e.g. [5]).

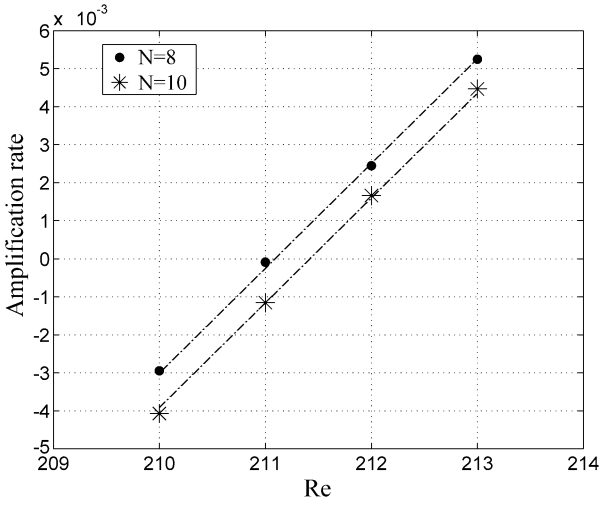

Fig. 5. Amplification rate versus Reynolds number for 8×8 and 10×10 collocation points.

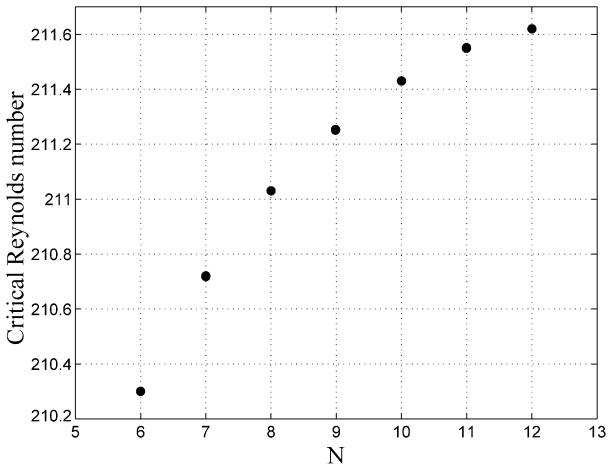

Fig. 6. Critical Reynolds number versus spatial discretization.

Table 1
Domain's dimension

L_{in}	$12d$
L_{out}	$25d$
Domain radius R	$8d$

Table 2
Critical Reynolds numbers with varying boundary conditions, with $N = 6$

Upstream length	Re_c	Number of elements
$12d$	210.30	169
$14d$	210.35	176
$18d$	210.35	183
Downstream length	Re_c	Number of elements
$30d$	210.30	169
$35d$	210.29	176
$40d$	210.30	183
$50d$	210.28	204
$60d$	210.29	218
Domain radius	Re_c	Number of elements
$8d$	210.30	169
$12d$	210.29	186

5.3. Amplification rate versus Reynolds number dependence

It was asserted in the beginning of this section that the amplification rate σ varies linearly close to the threshold of the instability. In Fig. 5, the amplification rates computed using N equal to 8 and 10 are plotted at different Reynolds numbers. The local linear behavior of the amplification rate is clearly made obvious.

It is interesting to note that the slope of the lines corresponding to 8×8 and 10×10 collocation points are the same. Fig. 5 thus shows that the derivative $\partial\sigma/\partial Re$, an important instability characteristic (see Sreenivasan et al. [24]), is easily accessible with reduced accuracy.

5.4. Influence of the geometrical parameters on the onset of the regular bifurcation

As previously discussed in Section 3.3, shifting the domain boundaries location could influence the instability development. Several tests of the geometrical parameters were performed to ensure that the outflow and inflow boundary conditions do not influence the onset mechanism of the primary bifurcation occurring for Reynolds numbers lying in the range of 210 and 212. In the upstream direction, the inflow condition was moved respectively to a distance of $12d$, $14d$ and $18d$ (d being the sphere diameter) from the sphere center, by adding one and two element layers while keeping the mesh size constant in the downstream and the lateral directions. The tests were carried out with 6×6 collocation points per element direction. The resulting critical Reynolds number variation is negligible, less than 0.03% in all cases.

In the same manner, the downstream domain extension was increased from $30d$ to $60d$, and the domain radius was changed from $8d$ to $12d$. The computed critical Reynolds number values associated to the regular instability are reported in Table 2. These numerical tests confirmed that extending the basic domain used in Ghidersa and Dušek [5] has no significant influence on the onset of the axisymmetry breaking.

5.5. Influence of the base flow accuracy

Kim and Pearlstein [1] warned of the necessity to have an accurate representation of the base flow, and to make certain of its convergence, since experimental work has shown the development of the instability to be sensitive to the details of the base flow. Therefore it is crucial that the base flow must be accurately computed. In order to confirm

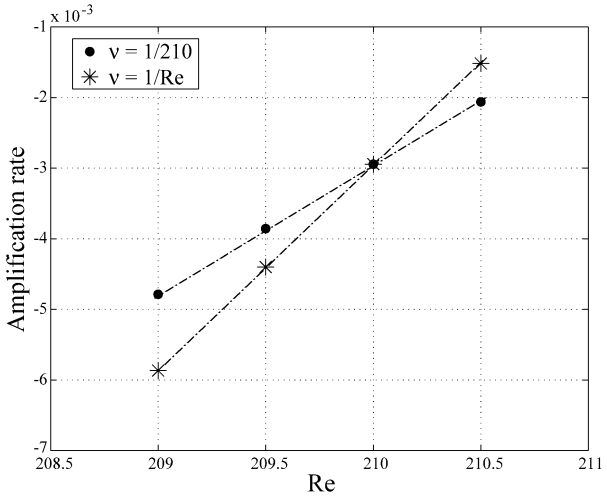

Fig. 7. Relative influence of the base flow and of viscosity on the amplification rate of the linear mode.

these warnings, the linear mode ($m = 1$) was computed at $Re = 210$ using base flows computed at several Re very close to 210. The amplification rates resulting from the calculation are presented in Fig. 7.

This figure shows that varying the axisymmetric base flow while keeping the viscosity at $Re = 210$ provides 2/3 of the change of the amplification rate σ. This allows to conclude that the base flow is crucial for the linear problem determination.

6. Steady non-axisymmetric flow

In Section 4, the steady axisymmetric flow was investigated between the onset of permanent vortex rings in the neighborhood of the rear stagnation point at $Re \approx 20$, to the threshold of the primary regular bifurcation determined to lie at $Re_{c_1} = 211.9$. This bifurcation leads to a steady non-axisymmetric flow regime. The flow assumes a planar symmetry and presents well-known characteristic features analyzed and explained exhaustively in [5]. The latter paper does not analyze the implication of axisymmetry breaking, and of planar symmetry on the hydrodynamic forces acting on the sphere. The loss of axisymmetry causes the onset of a lift force normal to the symmetry plane, and a torque perpendicular to the flow direction and to the symmetry plane. The drag, lift and torque are studied in the present section.

6.1. Computation accuracy

Using the Fourier expansion (5) and (6), Ghidersa and Dušek [5] proved that considering only 4 azimuthal modes suffices to describe with a very good precision the steady non-axisymmetric regime, and the transition to unsteadiness. Here, we consider up to 7 modes to investigate how the number of azimuthal modes influences the drag coefficient. To optimize the number of azimuthal modes allowing to reduce the CPU time without loss of information, we performed a test for a Reynolds number corresponding to the upper bound of the steady non-axisymmetric regime, which is the onset of the Hopf bifurcation.

Using 6×6 collocation points in the spatial discretization at $Re = 270$, evaluation of the drag C_D and lift C_L coefficients, (defined by $C_L = 8F_y/\pi D^2 \rho U_\infty^2$, F_y being the lateral force acting on the sphere) for each mode of the Fourier expansion, provided the results displayed in Fig. 8.

The drag coefficient saturates rapidly to a value reached with 4 modes (i.e. $m = 0, 1, 2$ and 3). Adding the 5th and 6th modes in the azimuthal expansion to the $m = 0$ through 4 modes increases the C_D value by less than 0.03% and the C_L value by less than 0.1%. Compared to the value computed with 5 modes [0–4], the underprediction occurring by considering only 4 modes does not exceed 0.25% for both quantities. Moreover, as found by Johnson and Patel [4], C_D is ten times higher than the lift coefficient C_L up to $Re = 300$. It can thus be concluded that for Reynolds ranging

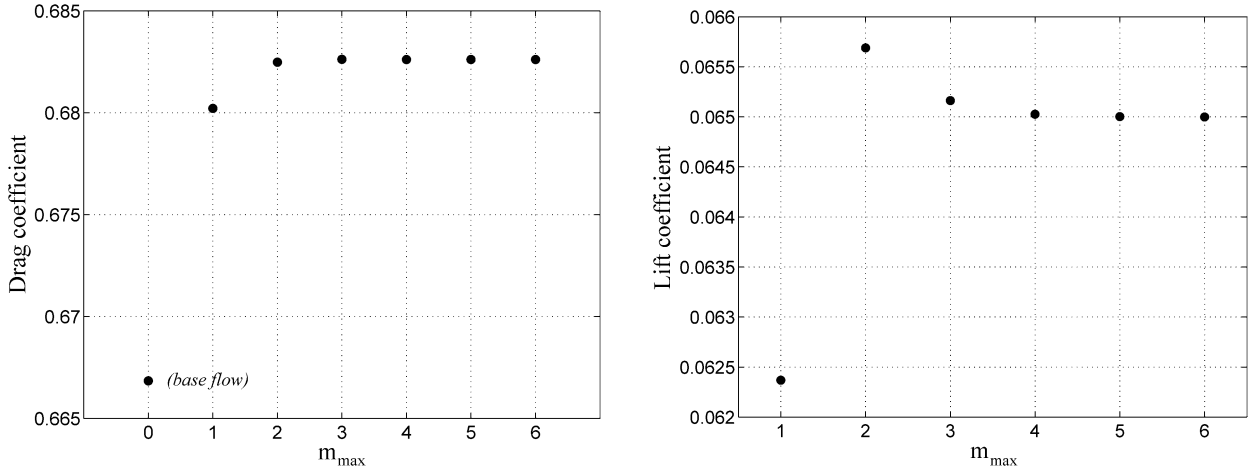

Fig. 8. Drag and lift coefficients versus number of azimuthal modes ($Re = 270$).

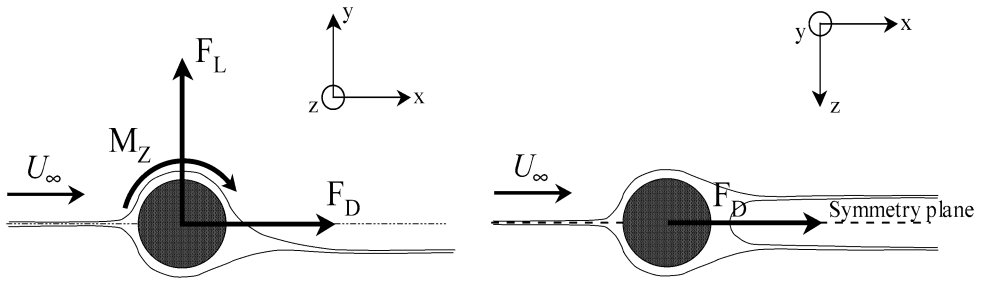

Fig. 9. Spatial axes system used to represent the forces and the torque.

between 212 and 270, taking account of more than 5 modes, brings no more relevant contribution to the drag and lift coefficients.

6.2. Drag, lift and torque

To obtain the drag and lift coefficients, as demonstrated in the previous paragraph, only 5 modes are necessary to reach both quantities with accuracy. To keep the CPU time within reasonable limits, the retained spatial discretization is a 8×8 collocation points in each macro-element. C_D and C_L are displayed in Figs. 10 and 11 (only values up to $Re = 274$ delimited by a vertical dashed line concern this section). No experimental measurements are available to confirm the lift coefficient values. The value at $Re = 250$ ($C_L = 0.0610$) compares well to that obtained by Johnson and Patel [4] ($C_L = 0.062$) by a different numerical method (finite differences). One notes also a good agreement with the results of Bagchi and Balachandar [22]. The non-dimensionalized torque coefficient $C_Z = 8M_z/\pi D^3 \rho U_\infty^2$ is related to M_z, the torque exerted by hydrodynamic forces on the sphere surface. The torque coefficient C_Z is also displayed versus Reynolds number in Fig. 11. The negative sign of the torque coefficient is due to the choice of axes. We put the x-axis in the asymptotic flow direction, the y-axis in the lift direction and the z-axis completes a direct coordinate frame. The lift arises due to a higher flow velocity in the positive direction of the y-axis. In the same time, the higher shear in this region of the sphere wall triggers a downstream rotation. Seen from the direction to which the z axis points, the rotation is clockwise (see the sketch in Fig. 9).

Fig. 11 reveals that the non-dimensionalized torque and the lift coefficient behave as the square root of the instability parameter $\epsilon = (Re - Re_c)/Re_c$, which results from that the fact that they are proportional to the amplitude of the fundamental mode (Figs. 10 and 11 present also time averaged coefficients C_D, C_L and C_Z in the unsteady periodic regime beyond $Re = 274$ discussed in Section 7).

In Fig. 10 we make it obvious how the axisymmetry breaking influences the drag coefficient. We present the values computed both for the axisymmetric base flow (obtained by forcing axisymmetry beyond the instability threshold)

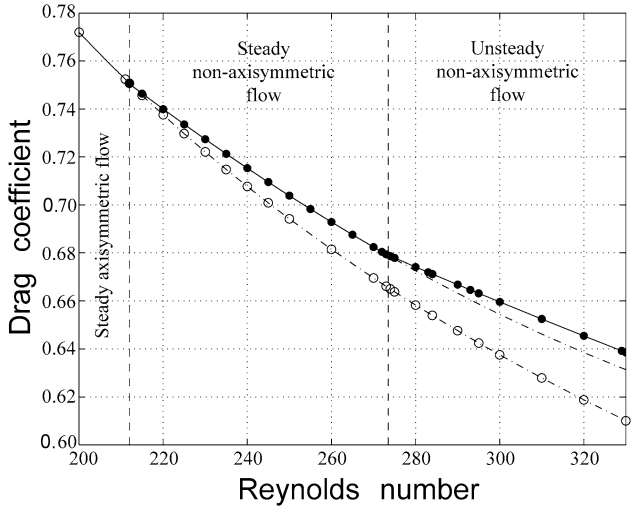

Fig. 10. Drag coefficient for Reynolds number ∈ [200–330] (○: forced axisymmetric flow; ●: total flow; the dash-dotted lines represent an extrapolation of the subcritical results).

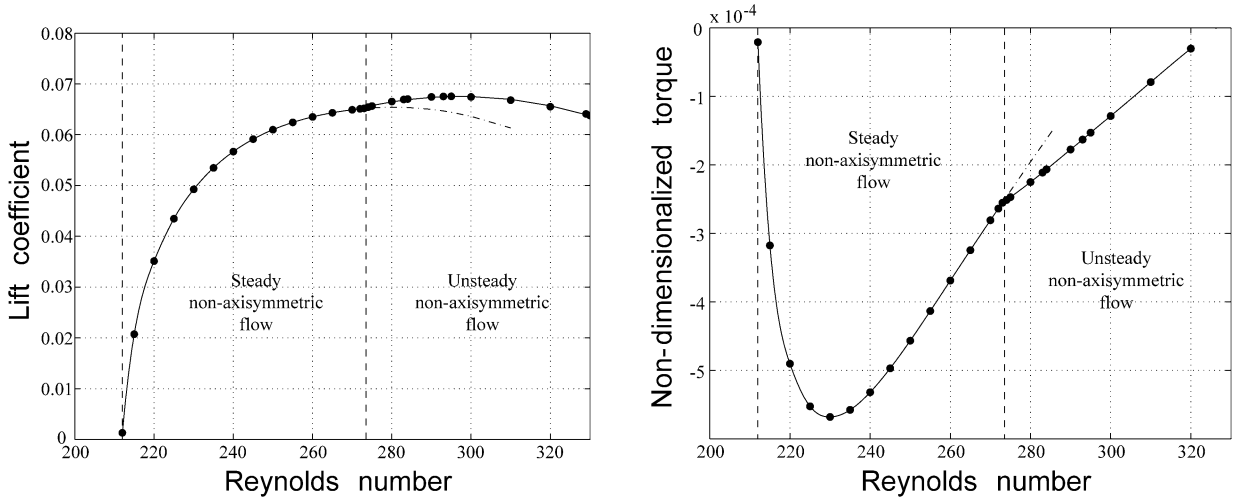

Fig. 11. Lift and non-dimensionalized torque coefficients for Reynolds number ∈ [200–330] (the dash-dotted lines represent an extrapolation of the subcritical results).

and for the (stable) non-axisymmetric flow. The difference increases with Reynolds number, and it is clear that the instability enhances the drag.

We also report a change in the curve of the recirculation length of the base flow compared to the axisymmetric base flow values, at the onset of the axisymmetry breaking. To extend the notion of recirculation length to the non-axisymmetric regime, we consider that of the flow averaged in the azimuthal direction. This flow is equivalent to the $m = 0$ azimuthal mode. Due to the non-linear interaction, the difference increases with the Reynolds number as shown in Fig. 12.

Fig. 13 allows to understand why the recirculation length stays practically constant above the instability threshold. The non-linear correction (the difference between the $m = 0$ mode and the axisymmetric base flow) which is due to the instability and increases proportionally to $\epsilon = (Re - Re_c)/Re_c$ just compensates the growth of the recirculation length of the base flow. The fact that instability enhances dissipation effects and, namely, reverses the increasing trend of the recirculation length has already been stated in the case of the Hopf bifurcation in the cylinder wake in [25]. The purpose of the extension of Figs. 10 and 11 beyond the threshold of unsteadiness is to further illustrate this fact in the next section. In contrast, the average separation angle defined as the separation of the $m = 0$ azimuthal mode

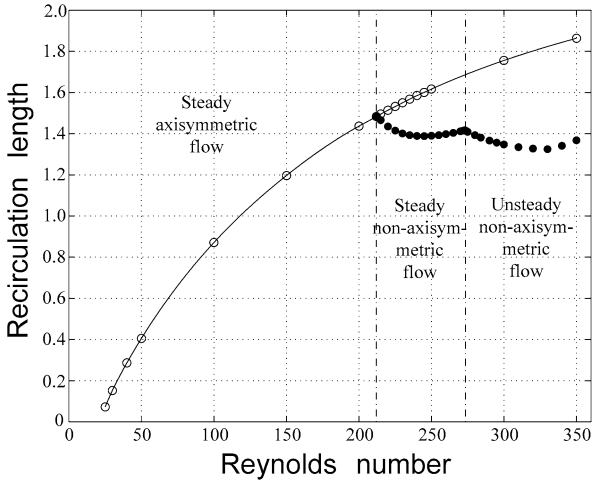

Fig. 12. Non-linear effects on the recirculation length (○: forced axisymmetric flow; ●: total flow).

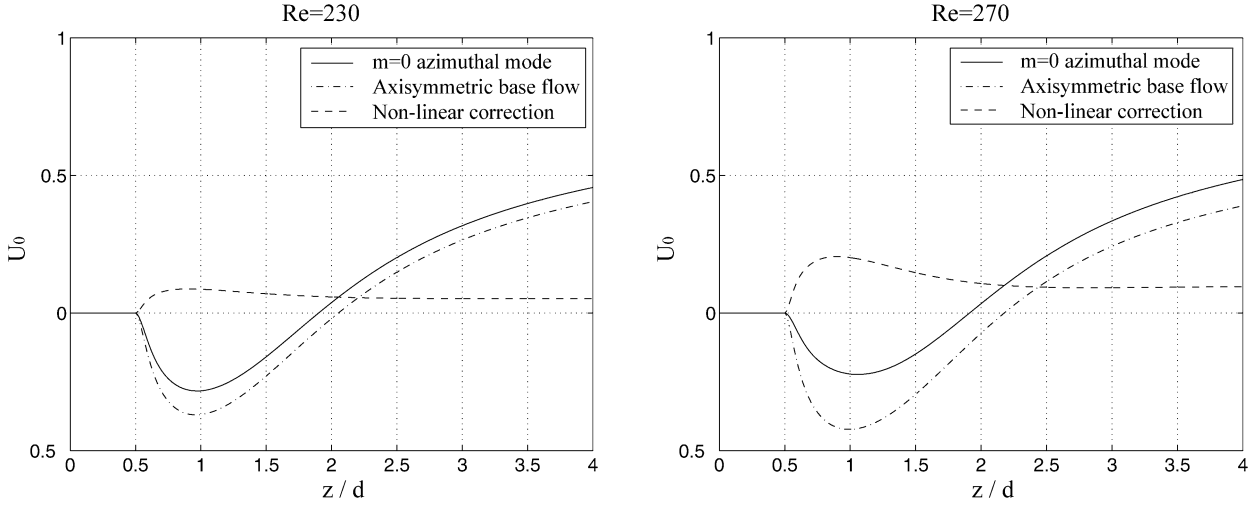

Fig. 13. Non-linear corrections on the axial velocity of the base flow.

Table 3
Separation angle for axisymmetric base flow and non-axisymmetric mean flow

Reynolds number	Axisymmetric base flow	Non-axisymmetric mean flow
215	115.54°	115.54°
230	114.25°	114.22°
270	112.94°	112.97°
300	112.41°	112.43°

is practically the same in presence and in absence of instability (see Table 3) because upstream of the rear stagnation point the amplitude of the latter is very weak.

7. Forces beyond the onset of unsteadiness

There is also a very good agreement between the experiments and the numerical simulations concerning the onset of unsteadiness in the sphere wake. The estimations of the critical Reynolds number given by several authors over the last years (Tomboulides et al. [3], Goldburg and Florsheim [26], Magarvey and Bishop [27], Sakamoto and Haniu [28],

Levi [16], Ghidersa and Dušek [5], Natarajan and Acrivos [2] and Jonhson and Patel [4]) converge to a value slightly below 275. For this Reynolds number value, the sphere wake undergoes a Hopf bifurcation leading from the steady non-axisymmetric flow to an unsteady periodic regime. The sphere wake starts to oscillate while keeping the symmetry plane selected by the first bifurcation. Therefore, the velocity and pressure components can be expressed in terms of a temporal Fourier series in each azimuthal subspace as:

$$v_m(r,z,t) = \sum_{n=-\infty}^{n=+\infty} c_{n,m}(r,z)\,\mathrm{e}^{\mathrm{i}n\omega t}, \tag{7}$$

$$p_m(r,z,t) = \sum_{n=-\infty}^{n=+\infty} d_{n,m}(r,z)\,\mathrm{e}^{\mathrm{i}n\omega t}. \tag{8}$$

Here we present the results of our numerical investigations of the periodic regime. Our simulations were carried out with a spatial discretization of 8×8 collocation points per spectral element, using 6 azimuthal modes [0–5] for $Re \in$ [274–290] and 7 modes [0–6] for the simulations at $Re > 290$. The choice of these discretization parameters results from tests of the numerical convergence of the oscillation amplitude. The present simulation allows to estimate the threshold of the Hopf bifurcation to lie below $Re_{c_2} = 274$, which is in very good agreement with the values commonly reported. Because of the unsteadiness, all three coefficients C_D, C_L and C_Z introduced in the previous section become oscillating quantities. To compare the trend below and above the Hopf bifurcation threshold we reported the time averaged values in the same Figs. 10 and 11 as the steady values below the threshold. The dash-dotted lines are just an extrapolation of the subcritical trend. The flow being periodic, an average over just one period is perfectly representative. Practically, the essential difficulty consists in reaching the limit cycle, which requires a simulation of several hundreds of periods, especially close to the threshold where the convergence is still slow. As a result 300 periods were simulated and the last 200 used for averaging. As can be seen, the trend of the Reynolds number dependence is systematically shifted towards higher dissipation effects by the instability. All the three coefficients would end up by having a smooth trend towards zero in the absence of the instability and the trend is retarded by a jump in the derivative. The explanation of the jump is straightforward. The plotted mean values represent the sum of the base flow (represented by the dash–dotted extrapolation) and of the non-linear mean value correction. The latter is a second effect, i.e. proportional to the square of the instability amplitude, which is, in its turn, proportional to the square root of the instability parameter $\epsilon = (Re - Re_{\mathrm{cr}})/Re_{\mathrm{cr}}$.

The linear trend in the right figure 11 representing the torque coefficient vs. the Reynolds number might convey the misleading conclusion that the torque reaches zero and even changes the sign immediately beyond $Re = 320$. This is, however, not the case because a next bifurcation reverses this trend at $Re = 325$.

Similarly as the first one, the second bifurcation allows to maintain the recirculation length practically constant (see Fig. 12) but does not affect the decrease of the separation angle . The forces oscillate with the same frequency as the wake characterized by the Strouhal number $St = fd/U_\infty$. In Fig. 14 the variation of the Strouhal number is plotted. The latter evolves relatively weakly with the Reynolds number but its values are very accurately accessible to experimental measures and represent, thus, a good validation for numerical computations. Ormières' [6] values for the threshold Strouhal number lying between 0.12 and 0.13 (depending on the experimental setup) and the published numerical values ($St = 0.136$ in [4] and [29], as well as $St = 0.135$ in [5] at $Re = 300$) are in a very good agreement with this figure.

The principal effects of the secondary instability are represented by the oscillation amplitude. As shown in Fig. 15, the lift coefficient oscillates with an amplitude about 4 times greater than C_D whereas the torque oscillates with an amplitude about 10 times smaller than C_D (in very good agreement with the results of Johnson and Patel [4] for $Re = 300$).

The amplitude modulation of the recirculation length seems to converge towards a value close to 20% of the mean value.

Our simulations evidence a further Hopf bifurcation accompanied by the onset of a second oscillation frequency of the wake at $Re = 325$. This second frequency is about 3 times smaller and this ratio appears to vary smoothly with the Reynolds number confirming a limit torus dynamics. Mittal [30] noted a similar phenomenon at $Re = 350$. Ormières [6] observed a second frequency at $Re \simeq 390$. Mittal reports, moreover, a loss of the plane symmetry and a chaotic behavior. This is in agreement with results obtained for a freely falling sphere in [31]. However, in this

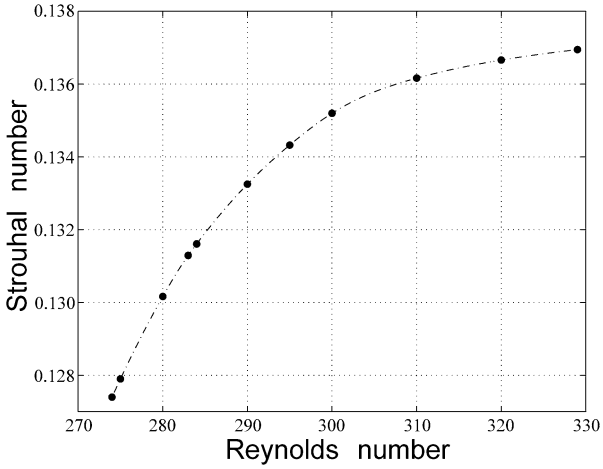

Fig. 14. Strouhal number versus Reynolds number for the secondary bifurcation.

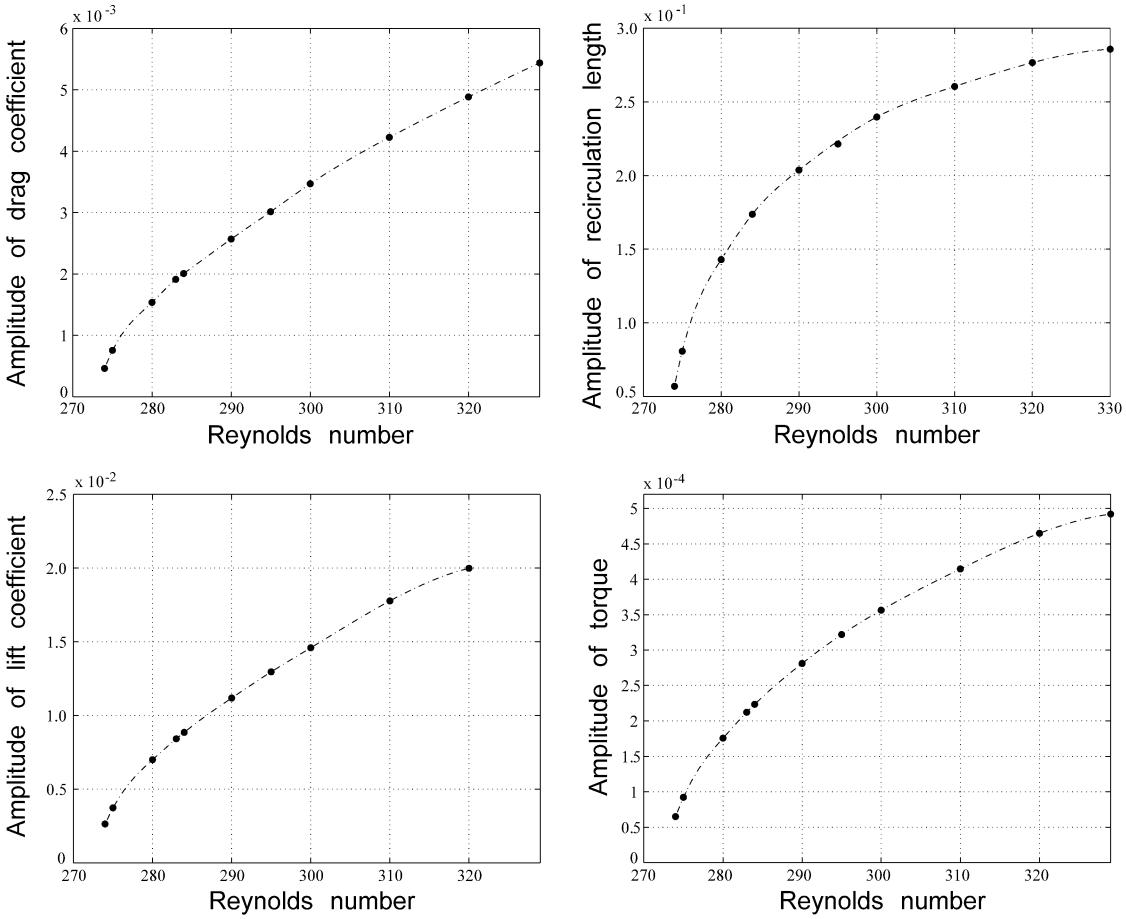

Fig. 15. Amplitude modulation of drag, lift and torque coefficients and amplitude modulation of the recirculation length.

last paper, it has been pointed out that the onset of three-dimensionality originates clearly in regular bifurcation. It seems thus somewhat strange to have a Hopf and a regular bifurcation setting in simultaneously. For this purpose we investigated the scenario of the transition to chaos and three-dimensionality for the fixed sphere wake in detail.

This work required a very fine analysis of the wake dynamics within a very narrow interval of Reynolds numbers and yielded interesting but fairly complex results the presentation of which goes far beyond the scope of the present paper and will be published elsewhere.

8. Conclusion

The onset of instabilities modifies considerably the action of the flow on a sphere. In addition to the drag, a lift and a torque appear as the axisymmetry breaks in the sphere wake. The lift and the torque become very soon appreciable. As far as the drag is concerned, the instability tends to increase it if compared to the drag in the unstable axisymmetric flow. The trend of the instabilities to increase the drag is further confirmed at the secondary instability yielding unsteadiness. In this regime, the force and torque become oscillating quantities with growing oscillation amplitudes. The mean values are significantly different from values extrapolated from the steady regime. The presented results are not yet fully pertinent from the point of view of particle trajectory because they do not allow to calculate the particle velocity and rotation due to the forces once the particle is set free. They give, nonetheless, an important hint that especially light particles are very likely to be strongly deviated from a straight trajectory and that the laminar phenomenological trajectory models are not valid beyond the primary instability onset.

References

[1] I. Kim, A.J. Pearlstein, Stability of the flow past a sphere, J. Fluid Mech. 211 (1990) 73–93.
[2] R. Natarajan, A. Acrivos, The instability of the steady flow past spheres and disks, J. Fluid Mech. 254 (1993) 323–344.
[3] A.G. Tomboulides, S.A. Orszag, G.E. Karniadakis, Direct and large-eddy simulation of axisymmetric wakes, in: AIAA – 31st Aerospace Sciences Meeting & Exhibit, 1993, pp. 1–12.
[4] T.A. Johnson, V.C. Patel, Flow past a sphere up to a Reynolds number of 300, J. Fluid Mech. 378 (1999) 19–70.
[5] B. Ghidersa, J. Dušek, Breaking of axisymmetry and onset of unsteadiness in the wake of a sphere, J. Fluid Mech. 423 (2000) 33–69.
[6] D. Ormières, Etude expérimentale et modélisation du sillage d'une sphère à bas nombre de Reynolds, PhD thesis, Université de Provence, 1999.
[7] L. Panton, Incompressible Flow, second ed., 1996.
[8] R. Clift, J.R. Grace, M.E. Weber, Bubbles, Drops and Particules, 1978.
[9] Y. Tsuji, Y. Morikawa, O. Mizuno, Experimental measurement of the Magnus force on a rotating sphere at low Reynolds numbers, Trans. ASME J. Fluids Engrg. 107 (1985) 484–488.
[10] J. Magnaudet, M. Rivero, J. Fabre, Accelerated flows past a rigid sphere or a spherical bubble. Part 1. Steady straining flow, J. Fluid Mech. 284 (1995) 97–135.
[11] A. Patera, A spectral element method for fluid dynamics: laminar flow in a channel expansion, J. Comput. Phys. 54 (3) (1984) 468–488.
[12] G.E. Karniadakis, Spectral element-fourier methods for incompressible turbulent flows, Comput. Methods Appl. Mech. Engrg. 80 (3) (1990) 367–380.
[13] R. Mittal, A Fourier–Chebyshev spectral collocation method for simulating flow past spheres and spheroids, Int. J. Numer. Methods Fluids 30 (1999) 921–937.
[14] S.A. Orszag, A.T. Patera, Secondary instability of wall bounded shear flows, J. Fluid Mech. 128 (1983) 347–385.
[15] R.H. Magarvey, R.L. Bishop, Transition ranges for three-dimensional wakes, Canad. J. Phys. 39 (1961) 1418–1422.
[16] E. Levi, Three-dimensional wakes: origin and evolution, J. Engrg. Division (1980) 659–676.
[17] S.C.R. Dennis, J.D.A. Walker, Calculation of the steady flow past a sphere at low and moderate Reynolds numbers, J. Fluid Mech. 48 (1971) 771–789.
[18] Y. Rimon, S.I. Cheng, Numerical solution of a uniform flow over a sphere at intermediate Reynolds numbers, Phys. Fluids 12 (5) (1969) 949–959.
[19] S. Taneda, Experimental investigation of the wake behind a sphere at low Reynolds numbers, J. Phys. Soc. Japan 11 (10) (1956) 1104–1108.
[20] I. Nakamura, Steady wake behind a sphere, Phys. Fluids 19 (1) (1976) 5–8.
[21] A.G. Tomboulides, S.A. Orszag, G.E. Karniadakis, Direct and large-eddy simulation of the flow past a sphere, in: Second International Conference on Turbulence Modeling and Experiments, 1993, pp. 1–10.
[22] P. Bagchi, S. Balachandar, Steady planar straining flow past a rigid sphere at moderate Reynolds number, J. Fluid Mech. 466 (2002) 365–407.
[23] F.W. Roos, W.W. Willmarth, Some experimental results on sphere and disk drag, AIAA J. 9 (2) (1971) 285–291.
[24] K.R. Sreenivasan, P.J. Strykowski, D.J. Olinger, Hopf bifurcation, Landau equation and vortex shedding behind circular cylinders, in: Proc. Forum on Unsteady Flow Separation, ASME Applied Mechanics, Bio Engineering Conference, Cincinnati, Ohio, June 11–17, ASME FED, 52, 1987.
[25] B.J.A. Zielinska, S. Goujon-Durand, J. Dušek, J.E. Wesfreid, A strongly nonlinear effect in unstable wakes, Phys. Rev. Lett. 79 (1997) 3893–3896.
[26] A. Goldburg, B.H. Florsheim, Transition and Strouhal number for the incompressible wake of various bodies, Phys. Fluids 9 (1) (1966) 45–50.
[27] R.H. Magarvey, R.L. Bishop, Wakes in liquid–liquid systems, Phys. Fluids 4 (7) (1961) 800–804.
[28] H. Sakamoto, H. Haniu, A study on vortex shedding from spheres in a uniform flow, Trans. ASME 112 (1990) 386–392.

[29] G.A. Tomboulides, S.A. Orszag, Numerical investigation of transitional and weak turbulent flow past a sphere, J. Fluid Mech. 416 (2000) 45–73.
[30] R. Mittal, Planar symmetry in the unsteady wake of a sphere, AIAA J. 37 (3) (1999) 388–390.
[31] M. Jenny, G. Bouchet, J. Dušek, Instabilities and transition of a sphere falling or ascending freely in a Newtonian fluid, J. Fluid Mech. 508 (2004) 201–239.